ELSEVIER

Journal of Fluids and Structures 19 (2004) 881–903

JOURNAL OF FLUIDS AND STRUCTURES

www.elsevier.nl/locate/jnlabr/yjfls

Numerical simulation of the interaction of a transitional boundary layer with a 2-D flexible panel in the subsonic regime

M.R. Visbal*, R.E. Gordnier

AFRL/VAAC, Bldg 146, Rm 225, 2210 Eighth St., Wright-Patterson AFB, OH 45433-7512, USA

Received 16 May 2002; accepted 1 May 2004

Available online 23 July 2004

Abstract

The self-sustained oscillations arising in subsonic transitional flow over a flexible finite panel are investigated numerically. The flowfields are obtained by solving the full compressible Navier–Stokes equations employing a recently developed sixth-order implicit code which is capable of retaining its superior accuracy on deforming meshes. The panel mechanics is described by means of the nonlinear von Karman plate equations which are solved with a previously validated structural module. An iterative implicit coupling of the fluid and structural solvers is provided in order to eliminate lagging errors at the fluid/solid interface. Computations are performed for two freestream Mach numbers ($M_\infty = 0.2, 0.8$), and for a range of Reynolds number and dynamic pressure. At both flow speeds, self-excited oscillations develop in the absence of an applied external forcing. At $M_\infty = 0.2$, the origin of the instability appears to be of an aeroelastic nature (i.e., flutter) and is found to persist even at very low Reynolds numbers. The fluctuating surface also generates boundary-layer instability modes downstream of the panel trailing edge. At the higher Mach number, static divergence occurs followed by the onset of travelling wave flutter (TWF), with frequency and wavelength compatible with those of Tollmien–Schlichting (T–S) waves. The observed limit-cycle oscillations appear to originate from the coupling of T–S waves with the higher-mode flexural waves on the elastic panel, and therefore subside below a critical value of Reynolds number. The TWF also generates significant acoustic radiation above the fluttering panel. The previous instabilities are observed for panels with either pinned or fully clamped edge conditions. Sensitivity of the solutions to the prescribed cavity pressure underneath the panel is noted. This dependence arises due to the different response of the boundary layer to the favorable or adverse pressure gradient induced by the upward or downward panel deflections, respectively.
Published by Elsevier Ltd.

Keywords: Panel flutter; Tollmien–Schlichting waves; von Karman plate model; Travelling wave flutter

1. Introduction

The complex flow–acoustic–structural interactions which may arise when a boundary-layer flows over an elastic or compliant surface are not only intriguing, but of significant importance in a variety of practical situations. These include panel flutter, transition delay, drag and noise reduction, turbulent flow sensing and modification, and control of unsteady separation by means of deforming flexible surfaces.

An extensive body of research exists on the subject of flow over flexible/compliant surfaces. This vast literature may be grouped for convenience in two major categories. The first category pertains to the field of aeroelasticity wherein the

*Corresponding author.
E-mail addresses: miguel.visbal@wpafb.af.mil (M.R. Visbal), raymond.gordnier@wpafb.af.mil (R.E. Gordnier).

0889-9746/$ - see front matter Published by Elsevier Ltd.
doi:10.1016/j.jfluidstructs.2004.05.001

Nomenclature

a	panel length
b	panel width
C_p	pressure coefficient
D	flexural stiffness, $E_s h^3/12(1-\nu^2)$
E	total specific energy
E_s	Young's modulus
f	frequency
$\hat{F}, \hat{G}, \hat{H}$	inviscid vector fluxes
$\hat{F}_v, \hat{G}_v, \hat{H}_v$	viscous vector fluxes
h	panel thickness
J	transformation Jacobian
K_f	linear free vibration frequency
l.e., *t.e.*	leading and trailing edge of flexible panel
M_∞	freestream Mach number
N'_x, N'_y, N'_z	membrane stresses
p	pressure
Re	Reynolds number, $\mathrm{Re} = \rho_\infty u_\infty a/\mu_\infty$
St	Strouhal number, $\mathrm{St} = fa/u_\infty$
t, τ	nondimensional time $\bar{t}u_\infty/a$
u, v, w	velocity components in x, y and z
x, y, z	physical coordinates
δ	boundary layer thickness
δ^*	displacement thickness
$\delta u, \delta v, \delta w$	structural displacements
ξ, η, ζ	computational coordinates
λ	dynamic pressure, $\rho_\infty u_\infty^2 a^3/D$; also wavelength
μ	viscosity coefficient
μ_s	mass ratio, $\rho_\infty a/\rho_s h$
ρ	density
ρ_s	panel density

phenomena of flutter and divergence of an elastic panel have been investigated for a number of years. An excellent review of the subject has been provided by Dowell (1970). The majority of the work on panel flutter has been based on linear (inviscid) aerodynamic models [e.g., Dowell (1966), Abdel-Motaglay et al. (1999)] which are suited for sufficiently high freestream Mach numbers but fail to provide reasonable predictions in the transonic regime. Potential flow theories aimed at providing predictions across the subsonic to supersonic Mach number range have been given by Dowell (1975). He also developed a shear flow model to account for viscous effects assuming a thin turbulent boundary-layer profile. For an extensive discussion of the theory, comparison with experimental measurements, as well as a complete citation of the original literature, the reader is referred to Dowell (1975).

Recently, Davis and Bendiksen (1993) have considered the nonlinear inviscid case by solving the two-dimensional (2-D) Euler equations coupled with a nonlinear finite-element model for a semi-infinite panel. They have also investigated travelling wave flutter at transonic conditions (Bendiksen and Davis 1995). Nydick et al. (1995) provided panel flutter solutions in the hypersonic regime employing a compressible Navier–Stokes solver, and compared their results with those obtained using third-order piston theory.

Gordnier and Visbal (2000, 2001) have further extended panel flutter simulations by considering both inviscid and viscous (laminar and turbulent) three-dimensional flow. In Gordnier and Visbal (2000), a well-validated flow solver has been coupled, via an iterative implicit strategy, with a finite-difference structural module for the nonlinear (von Karman) plate equations. This implicit coupling, which eliminates lagged-boundary-condition errors at the fluid–solid interface, has been found to be crucial in preventing spurious numerical instabilities of the combined nonlinear system. The same compressible Navier–Stokes flow solver was coupled with a finite-element structural solver by Gordnier and Fithen (2001).

The second category of previous research pertinent to the study of flow over flexible panels originates in the extensive field of laminar–turbulent transition delay by means of compliant coatings. The reader is referred to the classical papers by Kramer (1957), Benjamin (1963) and Landahl (1962), and to the recent reviews of Gad-el-Hak (1986) and Carpenter (1990). As described in these reviews, the coupling of two wave-bearing media engenders a variety of system instabilities including divergence, travelling wave flutter and the standard Tollmien–Schlichting (T–S) waves (modified by the wall compliance). Some of this complex instabilities have been classified (Gad-el-Hak 1986) according to either the fluid–solid energy exchange or their convective/absolute characteristics. The majority of related theoretical work in this arena deals with simplified flow models and small flexural deflections in a panel or coating of infinite length. Recent numerical simulation of the evolution of T–S waves over a finite panel has been given by Davies and Carpenter (1997).

The main objective of the present effort is the development of a high-fidelity methodology for the direct simulation of viscous flow past a flexible finite panel embedded in a rigid surface (see Fig. 1). Unlike previous computational work, the present approach considers the full three-dimensional compressible Navier–Stokes equations coupled with a nonlinear (von Karman) plate model for large transverse deflections. The flow fields are computed employing an implicit, sixth-order accurate code [Visbal and Gordnier (2000)] capable of retaining its superior accuracy on dynamic meshes, as required for flow simulation above the deforming panel. The structural solver of Gordnier and Visbal (2000) is incorporated and coupled through an implicit subiteration approach. The above methodology is then applied to the simulation of transitional boundary-layer flow over a 2-D flexible panel. Two different Mach numbers ($M_\infty = 0.2, 0.8$) and a range of Reynolds number and dynamic pressure are considered. The self-excited oscillations which emerge in the absence on an applied external forcing are described and are linked to the boundary-layer instability mechanism. The influence of the prescribed panel edge conditions and of the cavity pressure beneath the panel are also examined.

2. Governing equations

2.1. Flow equations

In order to properly account for the complex unsteady viscous flow arising over a dynamically deforming surface, the full compressible Navier–Stokes equations are selected. These equations are cast in a strong conservative form introducing a general time-dependent curvilinear coordinate transformation $(x, y, z, t) \rightarrow (\xi, \eta, \zeta, \tau)$. In vector notation, and employing nondimensional variables, the equations are:

$$\frac{\partial}{\partial \tau}\left(\frac{\vec{U}}{J}\right) + \frac{\partial \hat{F}}{\partial \xi} + \frac{\partial \hat{G}}{\partial \eta} + \frac{\partial \hat{H}}{\partial \zeta} = \frac{1}{\mathrm{Re}}\left[\frac{\partial \hat{F}_v}{\partial \xi} + \frac{\partial \hat{G}_v}{\partial \eta} + \frac{\partial \hat{H}_v}{\partial \zeta}\right]. \tag{1}$$

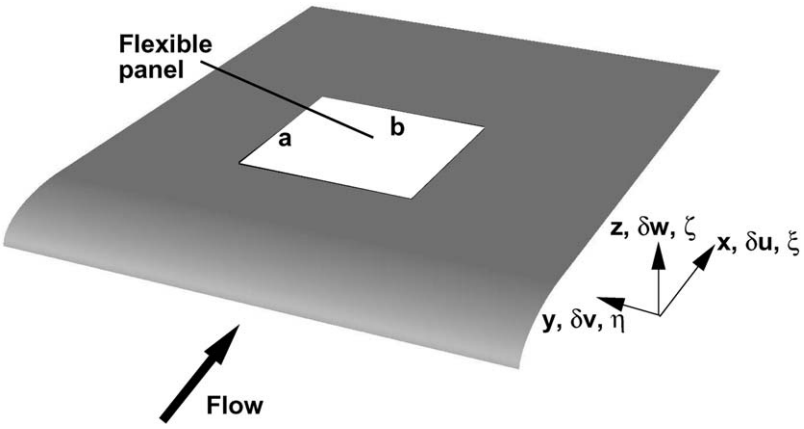

Fig. 1. Flexible panel geometry.

Here $\vec{U} = \{\rho, \rho u, \rho v, \rho w, \rho E\}$ denotes the solution vector, and J is the transformation Jacobian, which in general is a function of time. The inviscid fluxes $\hat{F}$, $\hat{G}$ and $\hat{H}$ are:

$$\hat{F} = \frac{1}{J}\begin{bmatrix} \rho U \\ \rho u U + \xi_x p \\ \rho v U + \xi_y p \\ \rho w U + \xi_z p \\ (\rho E + p)U - \xi_t p \end{bmatrix}, \tag{2}$$

$$\hat{G} = \frac{1}{J}\begin{bmatrix} \rho V \\ \rho u V + \eta_x p \\ \rho v V + \eta_y p \\ \rho w V + \eta_z p \\ (\rho E + p)V - \eta_t p \end{bmatrix}, \tag{3}$$

$$\hat{H} = \frac{1}{J}\begin{bmatrix} \rho W \\ \rho u W + \zeta_x p \\ \rho v W + \zeta_y p \\ \rho w W + \zeta_z p \\ (\rho E + p)W - \zeta_t p \end{bmatrix}, \tag{4}$$

where

$$U = \xi_t + \xi_x u + \xi_y v + \xi_z w, \tag{5}$$

$$V = \eta_t + \eta_x u + \eta_y v + \eta_z w, \tag{6}$$

$$W = \zeta_t + \zeta_x u + \zeta_y v + \zeta_z w, \tag{7}$$

$$E = \frac{T}{(\gamma - 1)M_\infty^2} + \frac{1}{2}(u^2 + v^2 + w^2). \tag{8}$$

The viscous fluxes, F_v, G_v and H_v can be found, for instance, in Anderson et al. (1984). In the expressions above, u, v, w are the Cartesian velocity components, ρ the density, p the pressure, and T the temperature. The perfect gas relationship $p = \rho T/\gamma M_\infty^2$ is also assumed. All flow variables have been normalized by their respective freestream values except for pressure which has been nondimensionalized by $\rho_\infty u_\infty^2$.

2.2. Structural equations for flexible panel

The deformations of the flexible surface are assumed to be governed by the (nonlinear) von Karman plate equations for large plate deflections. Derivation of these equations may be found in a number of sources, including Fung (1965) and Chia (1980). For the von Karman theory the plate is assumed to be isotropic, of uniform small thickness and initially flat. The normal deflection of the plate is assumed to be on the order of the thickness of the plate, while the tangential displacements are assumed infinitesimal. Finally, Kirchhoff's hypothesis is employed with tractions on surfaces parallel to the middle surface assumed negligible and strains varying linearly with the plate thickness.

Using these assumptions the governing equations for the plate motion may be written in nondimensional form as

$$\frac{\lambda}{\mu_s}\frac{\partial^2 \delta w}{\partial t^2} + \nabla^4 \delta w - \lambda N'_x \frac{\partial^2 \delta w}{\partial x^2} - 2.0\lambda N'_{xy}\frac{\partial^2 \delta w}{\partial x \partial y} - \lambda N'_y \frac{\partial^2 \delta w}{\partial y^2} = \frac{\lambda}{h}[p^u(x, y, t) - p_c], \tag{9}$$

$$\frac{\partial N'_x}{\partial x} + \frac{\partial N'_{xy}}{\partial y} = 0, \tag{10}$$

$$\frac{\partial N'_{xy}}{\partial x} + \frac{\partial N'_y}{\partial y} = 0, \tag{11}$$

where

$$N'_x = \frac{12.0}{\lambda}\left(\frac{\partial \delta u}{\partial x} + v\frac{\partial \delta v}{\partial y} + \frac{1}{2}\left[\left(\frac{\partial \delta w}{\partial x}\right)^2 + v\left(\frac{\partial \delta w}{\partial y}\right)^2\right]\right), \tag{12}$$

$$N'_y = \frac{12.0}{\lambda}\left(\frac{\partial \delta v}{\partial y} + v\frac{\partial \delta u}{\partial x} + \frac{1}{2}\left[\left(\frac{\partial \delta w}{\partial y}\right)^2 + v\left(\frac{\partial \delta w}{\partial x}\right)^2\right]\right), \tag{13}$$

$$N'_{xy} = \frac{12.0}{\lambda}\left(\frac{1-v}{2}\right)\left(\frac{\partial \delta u}{\partial y} + \frac{\partial \delta v}{\delta x} + \frac{\partial \delta w}{\partial x}\frac{\partial \delta w}{\partial y}\right). \tag{14}$$

The previous equations are written in a Lagrangian reference frame where x, y and z refer to the original undeflected plate location, and δu, δv and δw are the corresponding displacements from the undeflected position. The term $p^u(x, y, t)$ denotes the instantaneous fluid pressure acting on the upper surface of the plate, whereas p_c represents the pressure underneath the panel, which is typically assumed to be constant [Dowell (1975)]. These equations have been nondimensionalized based on the freestream density, freestream velocity and the length of the plate. The relevant nondimensional parameters are the panel aspect ratio a/b, the thickness ratio h/a, the mass ratio μ_s and the dynamic pressure λ (see Nomenclature).

Eqs. (9)–(11) form a coupled set of nonlinear equations for the plate deflections. The terms N'_x, N'_y, and N'_{xy} in Eq. (9) are the so called membrane stresses. These nonlinear terms arise due to the stretching of the middle surface of the plate.

It should be noted that the above structural equations could be easily extended to the more general case of a "Kramer-type" compliant surface or for a panel with a continuous elastic support. This can be accomplished through the addition of a structural damping term [of the form $\sim d(\partial \delta w/\partial t)$] and/or a restoring term ($\sim k\delta w$). Finally, the inclusion of externally applied axial forces could be accounted for by straight-forward modification of the membrane stresses N'_x, N'_y, N'_{xy}.

3. Numerical methodology

3.1. Flow solver

3.1.1. Spatial discretization

A finite-difference approach is employed to discretize the flow equations. For any scalar quantity, ϕ, such as a metric, flux component or flow variable, the spatial derivative ϕ' along a coordinate line in the transformed plane is obtained by solving the tridiagonal system:

$$\alpha\phi'_{i-1} + \phi'_i + \alpha\phi'_{i+1} = b\frac{\phi_{i+2} - \phi_{i-2}}{4} + a\frac{\phi_{i+1} - \phi_{i-1}}{2}, \tag{15}$$

where $\alpha = \frac{1}{3}$, $a = \frac{14}{9}$ and $b = \frac{1}{9}$. This choice of coefficients yields at interior points the compact five-point, sixth-order algorithm of Lele (1992). At boundary points 1, 2, $IL-1$ and IL, fourth- and fifth-order one-sided formulas are utilized which retain the tridiagonal form of the interior scheme [Gaitonde and Visbal (1998); Visbal and Gaitonde (1998)].

Compact-difference discretizations, like other centered schemes, are nondissipative and are therefore susceptible to numerical instabilities due to the growth of spurious high-frequency modes. These difficulties originate from several sources including mesh nonuniformity, approximate boundary conditions and nonlinear flow features. In order to ensure long-term numerical stability, while retaining the improved accuracy of the spatial compact discretization, a high-order implicit filtering technique [Gaitonde et al. (1997); Visbal and Gaitonde (1999b)] is incorporated. If a component of the solution vector is denoted by ϕ, filtered values $\hat{\phi}$ are obtained by solving the tridiagonal system,

$$\alpha_f\hat{\phi}_{i-1} + \hat{\phi}_i + \alpha_f\hat{\phi}_{i+1} = \sum_{n=0}^{N}\frac{a_n}{2}(\phi_{i+n} + \phi_{i-n}). \tag{16}$$

Eq. (16) is based on templates proposed in Lele (1992) and Alpert (1981), and with proper choice of coefficients, provides a $2N$th-order formula on a $2N+1$ point stencil. The coefficients, $a_0, a_1, \ldots, a_N$, derived in terms of the single parameter α_f using Taylor- and Fourier-series analyses, are given in Gaitonde and Visbal (1998), along with detailed spectral filter responses. In the present study, a tenth-order filter operator with $\alpha_f = 0.3$ is applied at interior points. For near-boundary points, the filtering strategies described in Visbal and Gaitonde (1999b) and Gaitonde and Visbal (1999) are employed. Filtering is applied to the conserved variables, and sequentially in each coordinate direction.

3.1.2. Metric evaluation

The extension of high-order schemes to nontrivial 3-D geometries demands that issues of freestream preservation and metric cancellation errors be carefully addressed. These errors, which arise in finite-difference discretizations of governing equations written in strong-conservation form, can catastrophically degrade the fidelity of higher-order approaches unless care is exercised in the treatment of the coordinate transformation metrics terms [Visbal and Gaitonde (1999a, b); Gaitonde and Visbal (1999)].

In deriving the strong-conservation flow equations, the following metric identities have been implicitly invoked:

$$I_1 = (\xi_x/J)_\xi + (\eta_x/J)_\eta + (\zeta_x/J)_\zeta = 0, \tag{17}$$

$$I_2 = (\xi_y/J)_\xi + (\eta_y/J)_\eta + (\zeta_y/J)_\zeta = 0, \tag{18}$$

$$I_3 = (\xi_z/J)_\xi + (\eta_z/J)_\eta + (\zeta_z/J)_\zeta = 0, \tag{19}$$

$$I_4 = (1/J)_\tau + (\xi_t/J)_\xi + (\eta_t/J)_\eta + (\zeta_t/J)_\zeta = 0. \tag{20}$$

The last metric identity (I_4) is referred to in the literature as the Geometric Conservation Law (GCL) [Thomas and Lombard (1979)] and becomes important in the case of deforming meshes such as those required in the present aeroelastic study. In a finite-difference discretization, these identities must also be satisfied numerically in order to ensure freestream preservation.

To numerically enforce identities I_1, I_2 and I_3 (Eq. (17)), the transformation metrics are evaluated in the manner described in Gaitonde and Visbal (1999) and Visbal and Gaitonde (1999b). In order to satisfy the GCL identity of Eq. (20), the time-derivative term in Eq. (1) is split using chain-rule differentiation as follows:

$$(\vec{U}/J)_\tau = (1/J)\vec{U}_\tau + \vec{U}(1/J)_\tau. \tag{21}$$

Rather than attempting to compute the time derivative of the inverse Jacobian directly from the grid coordinates at various time levels (either analytically or numerically), we simply invoke Eq. (20) to evaluate $(1/J)_\tau$, i.e.

$$(1/J)_\tau = -[(\xi_t/J)_\xi + (\eta_t/J)_\eta + (\zeta_t/J)_\zeta], \tag{22}$$

where

$$\begin{aligned}
\xi_t/J &= -[x_\tau(\xi_x/J) + y_\tau(\xi_y/J) + z_\tau(\xi_z/J)],\\
\eta_t/J &= -[x_\tau(\eta_x/J) + y_\tau(\eta_y/J) + z_\tau(\eta_z/J)],\\
\zeta_t/J &= -[x_\tau(\zeta_x/J) + y_\tau(\zeta_y/J) + z_\tau(\zeta_z/J)].
\end{aligned} \tag{23}$$

In general, the grid speeds are not known analytically, and must therefore be approximated to the desired degree of accuracy employing the evolving grid coordinates at several time levels. As previously shown in Visbal and Gordnier (2000), for dynamic meshes exhibiting rapid and severe distortion, second-order accuracy was found to be suitable for the evaluation of the grid speed terms x_τ, y_τ and z_τ. For the case of a flexible panel undergoing transverse deflections, the only relevant grid speed term is in the normal direction (see Fig. 2) and is expressed as

$$z_\tau = (3z^{n+1} - 4z^n + z^{n-1})/2\Delta\tau. \tag{24}$$

In the present aeroelastic simulations, the instantaneous shape of the deforming panel is obtained from the solution of the structural equations described earlier. In order to accommodate the panel vertical deflections, a new aerodynamic computational mesh is constructed at every time step, employing an efficient algebraic procedure. This is achieved by propagating the surface deformations into the mesh according to the following expression:

$$\begin{aligned}
z^{n+1}_{i,j,k} &= z^n_{i,j,k} + \delta z_{i,j,k},\\
\delta z_{i,j,k} &= \delta z_{i,j,1} G_{i,j,k},\\
G_{i,j,k} &= 1 - 3g^2_{i,j,k} + 2g^3_{i,j,k},\\
g_{i,j,k} &= s_{i,j,k}/s_{i,j,k_{\max}}, \quad 1 \leqslant k \leqslant k_{\max},
\end{aligned} \tag{25}$$

where $\delta z_{i,j,1}$ denotes the vertical displacement on the moving surface, s is the arc-length along the $\xi, \eta =$ constant lines, n is the time level, and $k_{\max}$ is the ζ-location in the far-field beyond which the mesh remains undeformed.

3.1.3. Time integration

For wall-bounded viscous flows, the stability constraint of explicit time-marching schemes is too restrictive, and the use of an implicit approach becomes necessary. For this purpose, the implicit approximately factored scheme of Beam and Warming (1978) is incorporated and augmented through the use of Newton-like subiterations in order to achieve

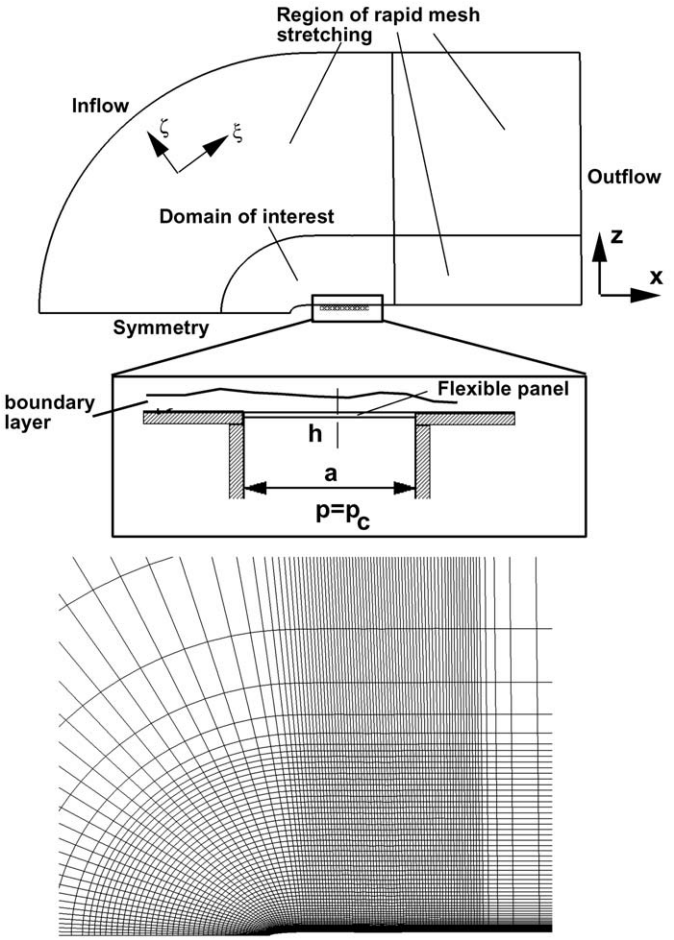

Fig. 2. Computational domain.

second-order time accuracy. In delta form, the scheme may be written as

$$\left[J^{-1^{p+1}}+\phi^i\Delta\tau\delta_\xi^{(2)}\left(\frac{\partial\hat{F}^p}{\partial U}-\frac{1}{\mathrm{Re}}\frac{\partial\hat{F}_v^p}{\partial U}\right)\right]J^{p+1}\left[J^{-1^{p+1}}+\phi^i\Delta\tau\delta_\eta^{(2)}\left(\frac{\partial\hat{G}^p}{\partial U}-\frac{1}{\mathrm{Re}}\frac{\partial\hat{G}_v^p}{\partial U}\right)\right]J^{p+1}$$
$$\times\left[J^{-1^{p+1}}+\phi^i\Delta\tau\delta_\zeta^{(2)}\left(\frac{\partial\hat{H}^p}{\partial U}-\frac{1}{\mathrm{Re}}\frac{\partial\hat{H}_v^p}{\partial U}\right)\right]\Delta U$$
$$=-\phi^i\Delta\tau\left[J^{-1^{p+1}}\frac{(1+\phi)U^p-(1+2\phi)U^n+\phi U^{n-1}}{\Delta\tau}+U^p(1/J)_\tau^p+\delta_\xi\left(\hat{F}^p-\frac{1}{\mathrm{Re}}\hat{F}_v^p\right)\right.$$
$$\left.+\delta_\eta\left(\hat{G}^p-\frac{1}{\mathrm{Re}}\hat{G}_v^p\right)+\delta_\zeta\left(\hat{H}^p-\frac{1}{\mathrm{Re}}\hat{H}_v^p\right)\right], \tag{26}$$

where

$$\phi^i=\frac{1}{1+\phi},\quad \Delta U=U^{p+1}-U^p. \tag{27}$$

For the first subiteration, $p=1$, $U^p=U^n$ and as $p\to\infty$, $U^p\to U^{n+1}$. The spatial derivatives in the implicit (left-hand side) operators are represented using standard second-order centered approximations, whereas high-order discretizations are employed for the explicit side. Although not shown in Eq. (26), nonlinear artificial dissipation terms (Jameson et al. 1981; Pulliam 1986) are appended to the implicit operator to enhance stability. In addition, for

improved efficiency, the approximately factored scheme is recast in diagonalized form (Pulliam and Chaussee 1981). Any degradation in solution accuracy caused by the second-order implicit operators, artificial dissipation and the diagonal form are eliminated through the use of subiterations. Typically, three subiterations are applied per time step. It should also be noted that further improvements in time accuracy could be achieved within the context of the present iterative approach by replacing the physical time-derivative, appearing on the right-hand side of Eq. (26), with a higher-order approximation (at the expense of additional levels of storage for the deforming grid coordinates and the dependent variables). However, based on the numerical tests of Visbal and Gordnier (2000), the second-order accuracy in time was found to be sufficient for the time steps typically employed.

3.2. Structural dynamics solver

The structural equations (Eqs. (9)–(11)) are solved using standard finite-difference procedures. All spatial derivatives are approximated using second-order accurate central differences. The time derivative is computed using Newmark's β method [Humar (1990)]. In this approach, the displacement, δw and velocity, $\delta \dot{w}$ are computed according to the following relations:

$$\delta \dot{w}^{n+1} = \delta \dot{w}^{n} + \frac{\Delta t}{2}(\delta \ddot{w}^{n} + \delta \ddot{w}^{n+1}), \tag{28}$$

$$\delta w^{n+1} = \delta w^{n} + \Delta t \delta \dot{w}^{n} + \frac{1}{2}(1-2\beta)\Delta t^{2}\delta \ddot{w}^{n} + \beta \Delta t^{2}\delta \ddot{w}^{n+1}. \tag{29}$$

In the present work, $\beta = \frac{1}{4}$ is used, which corresponds to a constant acceleration over a time interval (average acceleration method). This scheme is second-order accurate in time and unconditionally stable.

Substituting the appropriate finite-difference expressions and Eq. (29) into Eqs. (9)–(11) a set of difference equations is obtained. This system of equations is solved in an iterative fashion using a Gauss–Seidel solution technique. In this approach, Eq. (9) is uncoupled from Eqs. (10) and (11) by lagging the membrane stress terms. Similarly, all terms involving δw are assumed known when solving Eqs. (10) and (11). Successive over-relaxation is used with this iterative process in order to accelerate convergence which is assumed when the change in successive values of δw is less than a specified tolerance. The structural solver has been carefully validated [Gordnier and Visbal (2000)] for both static and dynamic loads.

3.3. Boundary conditions and fluid–structural coupling

The boundary conditions for the flow domain (see Fig. 2) are prescribed as follows. At the solid surface, the no slip condition is applied, requiring that the fluid velocity match the panel vertical velocity (i.e., $u = v = 0$, $w = z_\tau$). In addition, the wall is assumed to be isothermal ($T_w = T_\infty$), and the normal pressure gradient condition $\partial p/\partial n = -\rho \vec{a}_b \cdot \vec{n}$ is specified where $\vec{a}_b$ and $\vec{n}$ denote the surface acceleration and normal direction, respectively. Symmetry conditions ($w = 0, \partial(u, v, p, \rho)/\partial z = 0$) are employed on the plane $\xi = 0$ in front of the plate leading edge. For all the previous Neumann-type conditions, a fourth-order one-sided approximation is used.

The treatment of the far-field boundaries is based on the approach proposed and evaluated previously in Visbal and Gaitonde (2001) for some acoustic benchmark problems. This method exploits the properties of the high-order low-pass filter in conjunction with a rapidly stretched mesh (Fig. 2). As grid spacing increases away from the region of interest, energy not supported by the stretched mesh is reflected in the form of high-frequency modes which are annihilated by the discriminating spatial filter operator. An effective 'buffer' zone is therefore created using a few grid points in each coordinate direction without the need for the explicit incorporation of complicated boundary conditions or modifications to the governing equations. Since the acoustic radiation from the panel is damped prior to reaching the domain boundaries, simple boundary conditions can be applied. On the inflow boundary, uniform flow is specified, whereas at the outflow and side boundaries, all variables are extrapolated from the interior using a first-order extrapolation.

Boundary conditions for the plate are specified for either pinned or rigidly clamped edges. For either case, no deflection is allowed along the edges of the plate, i.e., δu, δv, $\delta w = 0$. For pinned edges, the additional zero-moment condition $\partial^2 \delta w/\partial n^2 = 0$ is specified (where n denotes the edge normal). In the case of a clamped panel, $\partial \delta w/\partial n = 0$, corresponding to zero slope at the edge.

The two-way fluid–structural coupling is provided through the time-varying loads exerted by the fluid on the plate (i.e., right-hand side of Eq. (9)), and through the transfer of the instantaneous panel deflections δw to the deforming aerodynamic mesh.

Since the same spatial discretization is used for both the fluid and the structure, no (spatial) interpolation technique is needed. However, the temporal coupling demands careful treatment. In the present numerical scheme, implicit coupling of these two sets of equations is achieved via the subiteration procedure previously described for the aerodynamic equations. By updating the aerodynamic forces in the structural equations and by providing the new surface displacement to the aerodynamic solver after each subiteration, the temporal lag between the aerodynamic and structural equations is eliminated. The importance of this synchronization between the fluid and the structural modules has been demonstrated previously (Gordnier and Visbal 2000) for the case of dynamic aeroelastic simulations.

4. Results

4.1. Preliminary considerations

Although the present computational approach has been developed for the general case of three-dimensional (3-D) flow past a finite-aspect-ratio (2-D) panel, only 2-D solutions for a semi-infinite ($a/b = 0$) panel are discussed in this paper. This is due to the fact that investigation of the many relevant nondimensional parameters involved (i.e., M_∞, Re_a, δ/a, λ, μ_s, a/b, h/a, p_c/p_∞) becomes computationally prohibitive in the full 3-D situation.

The flow configuration considered here is depicted in Fig. 2. An elastic panel is embedded in a flat surface along which a laminar boundary-layer develops. The panel of length a and thickness h extends over the region $0.5 \leqslant x/a \leqslant 1.5$. The leading-edge portion of the plate ($-0.5 \leqslant x/a \leqslant 0.0$) has been formed using an ellipse with half-thickness $0.05h$ (i.e., aspect ratio 10).

A baseline orthogonal computational mesh was generated algebraically employing elliptical cylindrical coordinates. In order to achieve the desired spacing, grid lines were redistributed and the resultant mesh was post-processed to provide improved smoothness using the GRIDGEN software. Two different grids of dimensions 206×187 (Grid 1) and 315×187 (Grid 2) were constructed. Grids 1 and 2 contain 51 and 101 points, respectively, over the panel. Description of the flow structure to be given below is based primarily on computed results obtained on the finer mesh. However, some parametric trends were studied employing only the coarser grid. Effects of grid resolution on the panel dynamics are provided in Section 4.3.2. A plot of Grid 2 is shown in Fig. 2 using every third line in both coordinate directions for the purpose of clarity. As discussed previously in Section 3.3, the grids are rapidly stretched beyond the chosen region of interest in order to provide an effective treatment of the far-field radiation conditions. Both meshes are stretched beginning at the streamwise location $x/a = 2.5$ using a constant stretching factor $\mathrm{SF} \approx 1.29$. After 21 points, this provides for Grid 1 an outflow boundary location at $x/a \approx 23$. The normal grid distribution (common to both meshes) is obtained by clustering coordinate lines next to the surface using an exponential stretching with a minimum spacing $\Delta z/a = 5.0 \times 10^{-5}$ at the wall. Typically, 50 points are contained within the boundary layer (at the leading edge of the panel) which provides ample resolution using the present sixth-order flow solver (Visbal and Gaitonde 1999b). The grid is again rapidly stretched in the normal direction ($\mathrm{SF} \approx 1.3$) beyond $z/a = 2.65$. With 25 points, this results in a far-field boundary location of $z/a \approx 100.0$ above the plate.

4.2. Rigid-plate solutions

Solutions corresponding to a *rigid* panel were first obtained for freestream Mach numbers $M_\infty = 0.2$ and 0.8, and for a Reynolds number $\mathrm{Re}_a = 1.0 \times 10^5$ based on panel length ($\mathrm{Re} = 5.0 \times 10^3$ in terms of the half-thickness of the elliptical leading edge). Unlike the case of receptivity studies [e.g., Buter and Reed (1994)], in the present simulations no perturbations were imposed to trigger boundary-layer transition, and therefore, steady solutions were achieved above the rigid panel.

The computed surface pressure along the plate is displayed in Fig. 3 for both Mach numbers. For $M_\infty = 0.2$, a zero-pressure gradient flat-plate boundary layer is effectively obtained over the panel. The computed results are in good agreement with Blasius solution in terms of the displacement thickness growth (Fig. 4) and the streamwise velociy profile (Fig. 5). For $M_\infty = 0.8$, however, a residual adverse pressure gradient persists in the panel region (Fig. 3) and results in perceptible changes in the boundary-layer velocity profile (Fig. 5) (with an inflection point at $z/\delta \approx 0.31$). Although this pressure gradient effect could be diminished by locating the panel further downstream, this was not pursued due to the consequent increase in the size of the computational domain. A summary of the boundary-layer characteristics for the rigid-plate solutions is provided in Table 1. The ratio of the panel length to the boundary-layer thickness at the trailing edge of the panel is approximately 40 for both freestream Mach numbers.

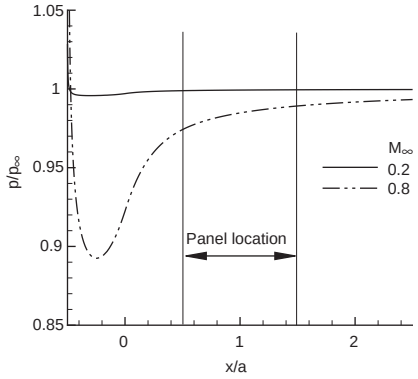

Fig. 3. Surface pressure distribution for rigid-plate solutions.

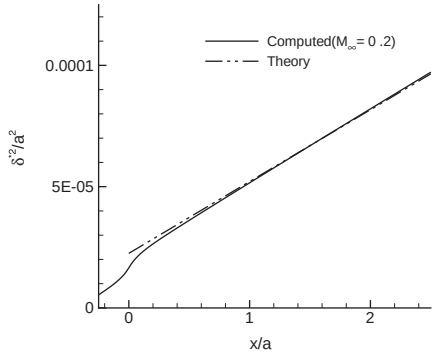

Fig. 4. Boundar-layer displacement thickness growth along rigid plate ($M_\infty = 0.2$, $\mathrm{Re}_a = 10^5$).

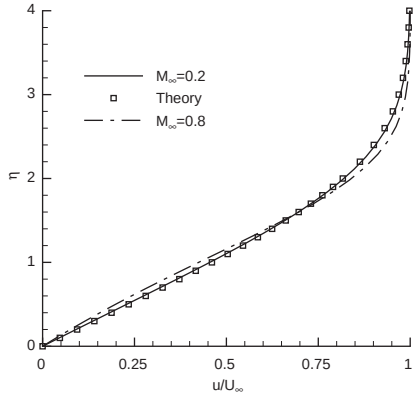

Fig. 5. Boundary-layer velocity profiles for flow over rigid panel at $x/a = 1.0$.

Table 1
Rigid-plate boundary layer parameters

M_∞	x/a	δ/a	δ^*/a	Re_{δ^*}	p/p_∞
0.2	0.5	0.018	0.0060	601	0.9989
0.2	1.5	0.025	0.0082	818	0.9995
0.8	0.5	0.021	0.0071	707	0.9742
0.8	1.5	0.027	0.0091	910	0.9892

4.3. Flexible-panel solutions

Calculations of the interaction of the laminar boundary layer with the flexible panel were studied for two freestream Mach numbers ($M_\infty = 0.2, 0.8$). For the elastic isotropic panel, the following structural baseline parameters were specified: aspect ratio $a/b = 0$, plate thickness $h/a = 0.002$, mass ratio $\mu_s = 0.1$ and Poisson ratio $\nu = 0.3$. The dynamic pressure λ ranged from 10 to 500. Unless noted otherwise, pinned conditions were prescribed at both edges of the panel. In all cases, the corresponding rigid-plate solutions were specified as initial conditions. In order to minimize static deflections, the cavity pressure underneath the panel was set equal to the streamwise-average value obtained from the rigid-plate solutions and defined as $p_c = \frac{1}{2}(p_{le} + p_{te})$ (see Table 1). It should be noted that no initial perturbations were imposed on either the boundary layer or the flexible panel to promote a fluid/structure interaction. Instead, the interaction was allowed to evolve from the small pressure differences existing above and below the panel coupled with the natural instabilities of the combined system.

4.3.1. Results for $M_\infty = 0.2$

The history of the transverse deflections δw at the panel quarter-chord point is shown in Fig. 6(a) for a dynamic pressure $\lambda = 500$. As the flexible panel is allowed to deform, the small pressure differential existing between the outer flow and the cavity initiates the panel fluctuations. At early times (nondimensional time $t < 50$, Fig. 6(b)), these oscillations are characterized by a low frequency of order $3K_f$ where K_f denotes the fundamental linear structural frequency of the panel. By $t \approx 50$, an increase in fluctuation frequency is already apparent. However, it is only after a very long transient ($t > 200$) that the panel response eventually asymptotes to a self-sustained, high-frequency oscillatory pattern (Fig. 6(c)). A spectrum of the fluctuations, shown in Fig. 7, displays a well-defined peak at $\mathrm{St} = fa/U_\infty = 0.44$. The ratio of St to the panel fundamental linear frequency (K_f) is approximately 20 and is considerably larger than the values typically encountered in supersonic inviscid panel flutter (Dowell 1970; Gordnier and Visbal 2001; Davis and Bendiksen 1993). From the phase plot of Fig. 6(d), the panel deflections are observed to be centered about the panel equilibrium position indicating insignificant effects of either aeroelastic divergence or plain static deformation, the latter being avoided by the properly selected cavity pressure. The peak transverse deflection of the panel at the quarter-chord point shown reaches approximately 3.6 times the panel thickness. In addition, the maximum vertical velocity fluctuations are of order $0.02U_\infty$. Therefore, from both the structural and boundary-layer transition perspectives, the present fluid–structure interaction can be considered to be highly nonlinear. In fact, if a *linear* structural model is employed (by neglecting the in-plane stresses), the computed panel deflections grow unbounded until the solution procedure becomes numerically unstable.

A plot of the instantaneous panel shape, shown in Fig. 8(a), indicates that the predominant transverse oscillations of the fluttering panel correspond to a stationary second-mode pattern. In order to illustrate this feature more clearly, the panel deflections were recorded for a sufficient length of time and are plotted in the $x - t$ diagram of Fig. 9(a), where the second-mode panel oscillations are quite discernable and repeatable. The evolution of the surface pressure on the panel

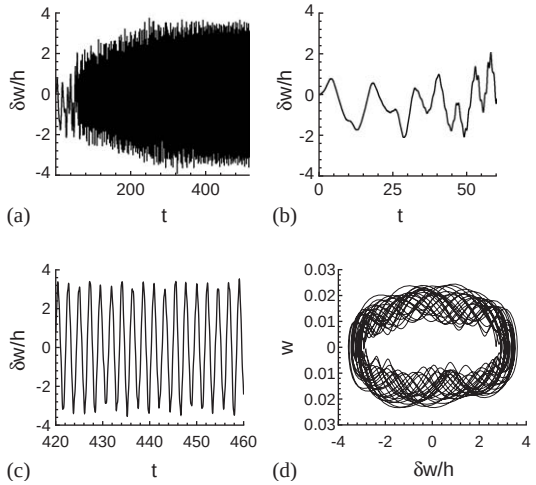

Fig. 6. History of panel transverse deflection and velocity at the quarter-chord point ($M_\infty = 0.2$, $\lambda = 500$).

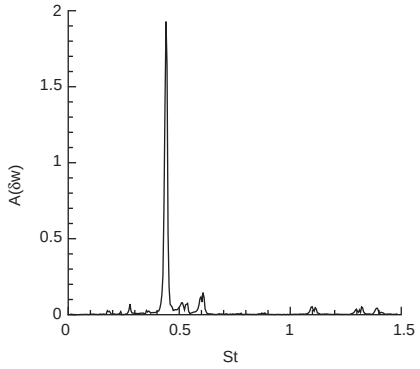

Fig. 7. Spectrum of panel fluctuations ($M_\infty = 0.2$, $\lambda = 500$).

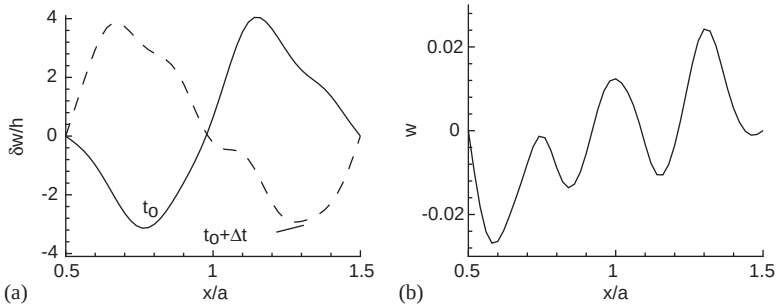

Fig. 8. Instantaneous panel shape (a) and vertical velocity (b) ($M_\infty = 0.2$, $\lambda = 500$, $\Delta t = 1.06$).

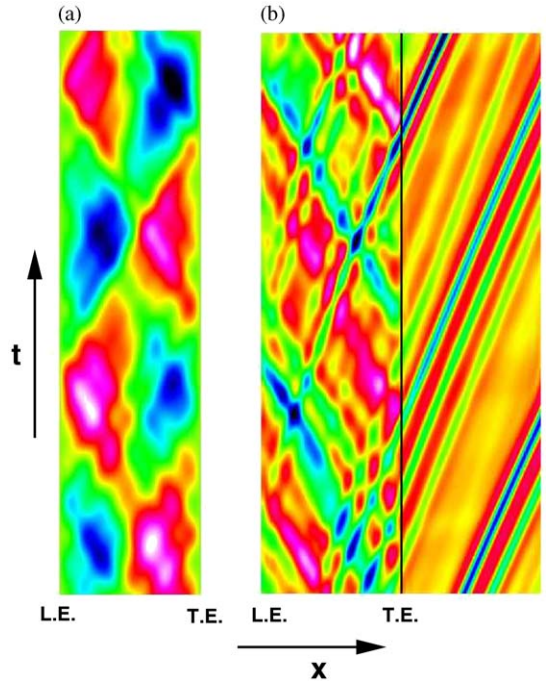

Fig. 9. x–t Diagram of panel deflection (a) and surface pressure (b) ($M_\infty = 0.2$, $\lambda = 500$).

(Fig. 9(b)) points out the existence of an additional higher-mode component evidenced by the instantaneous transverse panel velocity w (Fig. 8(b)).

The instantaneous structure of the flow above the panel is shown in Fig. 10 in terms of contours of the velocity components (u, w) and the spanwise vorticity (ω_y). It should be noted that the vertical scale in Figs. 10(b) and (c) has been enlarged by a factor of 10 for the purpose of clarity. Downstream of the plate trailing edge, the development of instability waves is apparent in Figs. 10(a) and (b). These disturbances propagate downstream at an approximate phase speed $c_r/U_\infty = 0.42$ as can be inferred from the $x - t$ diagram of Fig. 9(b). The instability wave train (Fig. 10) is not entirely regular in the streamwise direction. By examination of the flow structure at many instants it became apparent that stronger vortical disturbances (denoted as '1' in Fig. 10(b)) emerge near the panel trailing-edge at the dominant frequency of the transverse vibrations. The wavelength associated with these larger disturbances is of order $\lambda_1/a = 0.9$. The interaction of the stronger disturbances with the near-surface flow results also in the generation of secondary structures (of opposite signed vorticity) and in small pockets of reversed flow. The weaker vortical structures (denoted as '2') have a wavelength $\lambda_2/a \approx 0.2$ and appear to correspond to the T–S waves. The value of λ_2 is approximately equal to eight times the nominal boundary-layer thickness at the trailing edge of the panel (Table 1). The effect of the passage of the vortical structures on the surface pressure history at $x/a = 2.5$ is shown in Fig. 11. The pressure signal exhibits two dominant frequencies ($St_1 \approx 0.43$, $St_2 \approx 2.4$) in accordance with the observed character of the vortical flow.

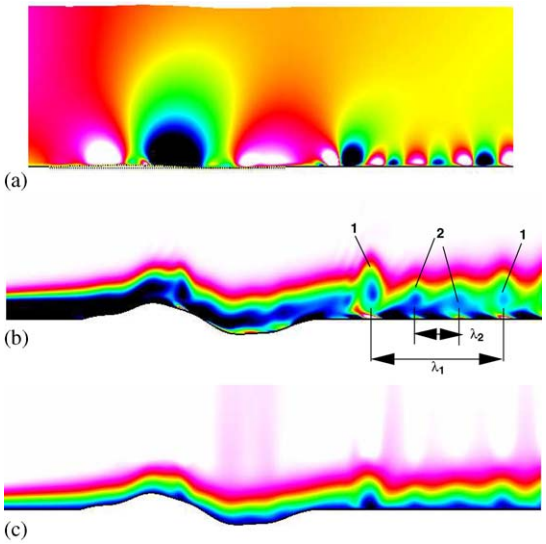

Fig. 10. Instantaneous flow structure above flexible panel in terms of contours of (a) normal velocity, (b) spanwise vorticity and (c) streamwise velocity. The vertical scale in (b,c) has been enlarged by a factor of 10 ($M_\infty = 0.2$, $\lambda = 500$).

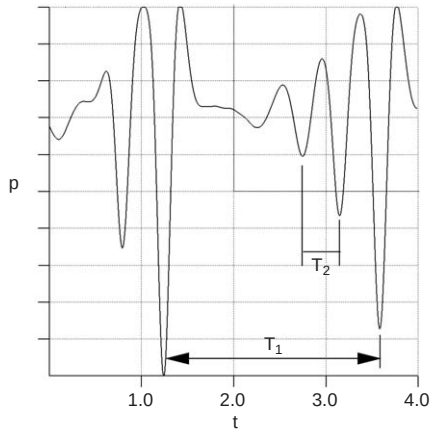

Fig. 11. Pressure signal on plate surface at $x/a = 2.5$ ($M_\infty = 0.2$, $\lambda = 500$).

The nature of the unsteady flow near the plate is presented in Fig. 12 using contours of the root-mean-square of the fluctuating pressure and a profile of the streamwise and normal velocity fluctuations in the boundary layer at a station downstream of the panel ($x/a = 2.0$). The acoustic radiation above the surface (Fig. 12(a)) displays a two-lobe pattern consistent with the dominant second-mode flexural vibration of the panel. The value of $\sqrt{\overline{u'^2}}$ reaches a maximum of 0.077 at $z/\delta = 0.22$ which represents a high-level of turbulent fluctuations in the boundary layer following its encounter with the elastic panel.

It is of interest to examine the relationship of the panel oscillations to the instability modes (T–S waves) of the laminar boundary layer. For this purpose, the observed frequencies are compared with the classic theoretical results [Schlichting (1968)] for an incompressible flat-plate boundary layer. Fig. 13 displays the curve of neutral stability for the nondimensional disturbance frequency $\beta_r\delta^*/U_\infty$. As noted earlier, in the present fluid–structure interaction at $M_\infty = 0.2$, two distinct frequencies (St_1, St_2) are found in the boundary-layer disturbances downstream of the fluttering panel. These are plotted as individual points in Fig. 13 using as reference the displacement thickness at the trailing edge of the panel (Table 1). The lower frequency ($St_1 = 0.43$, $\beta_r\delta^*/U_\infty = 0.02$), which correlates with the panel transverse fluctuations (Fig. 7), clearly falls outside the region of instability. On the other hand, the higher-frequency mode ($St_1 = 2.4$, $\beta_r\delta^*/U_\infty = 0.124$) falls within the two neutral stability branches. Therefore it appears that two separate

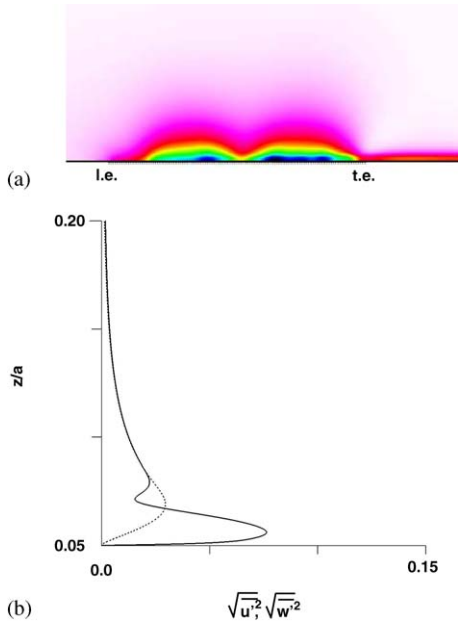

Fig. 12. Contours of RMS-pressure fluctuations above the panel (a) and boundary-layer velocity fluctuations at $x/a = 2.0$ (b) ($M_\infty = 0.2$, $\lambda = 500$).

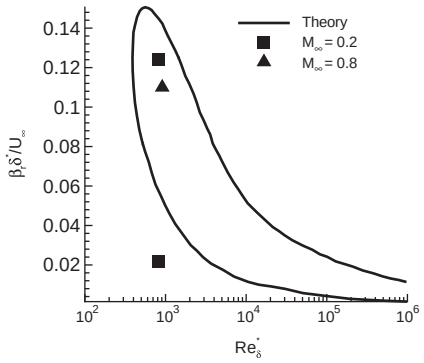

Fig. 13. Comparison of computed frequencies with stability analysis for a flat-plate incompressible boundary layer.

processes are at play in this particular self-excited oscillatory phenomenon. The lower-frequency oscillations are likely to represent an (absolute) aeroelastic instability (flutter) of the coupled fluid/structural system and it is not caused by the growth of T–S waves over the flexible panel. The validity of this assertion is explored later by performing calculations at much lower Reynolds numbers where flutter is found to persist for Re^*_δ as low as 200. The higher-frequency oscillations appear to correspond to the convective boundary-layer instability modes being excited by the flexural vibration of the panel.

Parametric effects. The effect of the dynamic pressure parameter λ on the fluid–structure interaction is considered in Figs. 14–16 which display the mean panel deflection, deflection amplitude and maximum transverse velocity at the

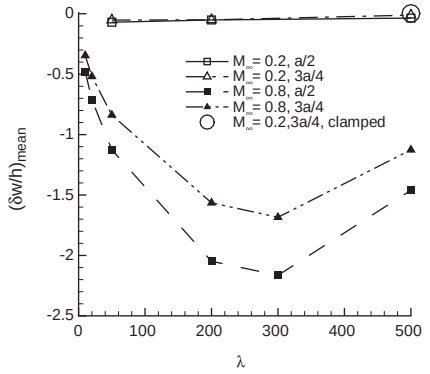

Fig. 14. Effect of dynamic pressure on mean panel deflection.

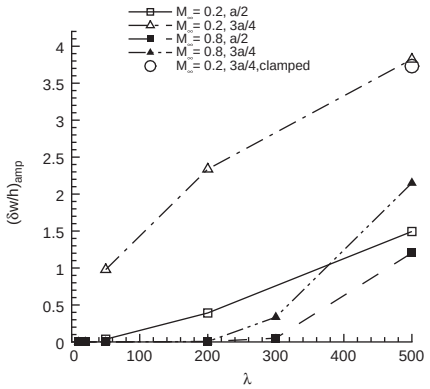

Fig. 15. Effect of dynamic pressure on oscillation amplitude.

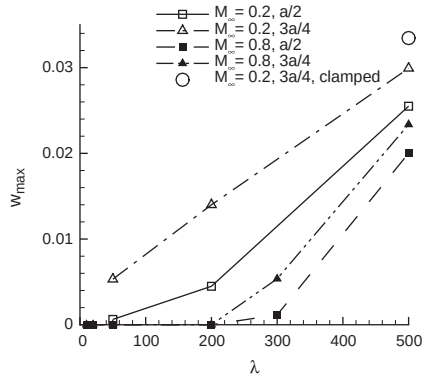

Fig. 16. Effect of dynamic pressure on panel maximum transverse velocity.

midchord and $\frac{3}{4}$-chord panel stations. These results were obtained employing the coarser mesh which is expected to provide sufficient resolution for examination of the qualitative trends. Over the range $50 \leqslant \lambda \leqslant 500$, the panel mean deflection at both sampling points (Fig. 14) is very close to the original equilibrium position ($z = 0$). The small mean deflections observed are less than 0.05 times the panel thickness and indicate the absence of significant aeroelastic divergence. Instead, the panel oscillates about $z \approx 0$ with amplitude (Fig. 16) and transverse velocity (Fig. 15) which increase with λ. The deflection amplitude is considerably larger at the $\frac{3}{4}$-chord location (Fig. 15) consistent with the predominance of a second-mode flutter in the panel dynamics. A more detailed examination of the panel response also revealed that with increasing λ there is a strengthening of the higher-mode travelling wave flutter component previously noted.

Next, in order to investigate the effect of the structural boundary conditions on flutter, a computation was also performed for $\lambda = 500$ using clamped conditions at both ends of the panel. The results, plotted in Figs. 14–16, indicate very small changes relative to the previous pinned-edge calculations. In addition, comparison of the flow fields (not shown) revealed the same unsteady structure and demonstrates that the observed flutter phenomena is fairly independent in this case from the prescribed panel edge-conditions.

Finally, the effect of Reynolds number on the computed self-excited oscillations was considered by varying the specified value of Re_a. Fig. 17 displays the amplitude of the transverse fluctuations at the $\frac{3}{4}$-chord station as a function of Re_δ^* (based on the reference condition at the panel leading edge). The limit-cycle-oscillation phenomenon does not disappear for lower Reynolds number. In fact, the amplitude of the fluctuations increased with decreasing Reynolds number over the range $200 < \mathrm{Re}_\delta^* < 600$ ($10^4 < \mathrm{Re}_a < 10^5$) even though the minimum Re_δ^* is significantly lower than the critical value $\mathrm{Re}_{cr} = 420$. This behavior confirms the previous assertion regarding the origin of the aeroelastic instability as being separate from the T–S waves.

4.3.2. *Results for* $M_\infty = 0.8$

The history of the transverse deflections at the quarter-chord point is shown in Fig. 18 for a freestream Mach number $M_\infty = 0.8$ and dynamic pressure $\lambda = 500$. Similar to the previous low-speed case, the time scales associated with the dynamics of the structure result in a very long transient prior to the establishment of a self-sustained oscillation of the combined system. The spectrum of the flexural fluctuations, given in Fig. 19 ($\Delta t = 0.0025$), indicates a dominant frequency $\mathrm{St} = 1.52$ which is again considerably higher than the fundamental frequency of the elastic plate. The panel oscillates about a downward mean deflected position with maximum amplitude at the quarter-chord of approximately $0.5h$ and maximum vertical velocity of order $0.01U_\infty$.

The instantaneous panel shapes, shown in Fig. 20(a), display a seventh-mode deflection superimposed on a first-mode (static) divergence. The higher-mode deflections are observed to travel along the panel. The character of this travelling wave flutter is seen more clearly in the $x - t$ plot of Figs. 21(a,b) where the flexural deflections are observed to propagate (with approximate phase speed $0.44U_\infty$) and to reflect at the edges of panel.

The instantaneous flow structure above and downstream of the fluttering panel is presented in Fig. 22 in terms of the pressure, normal velocity component and spanwise vorticity. The pressure contours (Fig. 22(a)) reveal significant acoustic radiation generated above the panel by the travelling wave flutter. These acoustic waves extend over the entire domain of interest and exit into the buffer zone (stretched-mesh region) without producing noticeable reflections. Downstream of the panel, the boundary-layer instability waves are quite apparent (Fig. 22(b) and (c)). In contrast with the results for $M_\infty = 0.2$, the pattern of vortical structures is quite regular downstream of the plate trailing edge. The

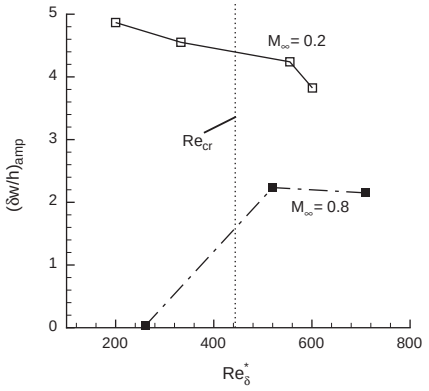

Fig. 17. Effect of Reynolds number on oscillation amplitude at the panel $\frac{3}{4}$-chord.

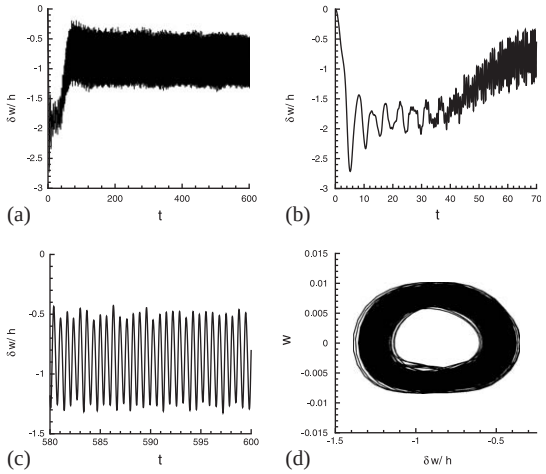

Fig. 18. History of panel transverse deflection and velocity at the quarter-chord point ($M_\infty = 0.8$, $\lambda = 500$).

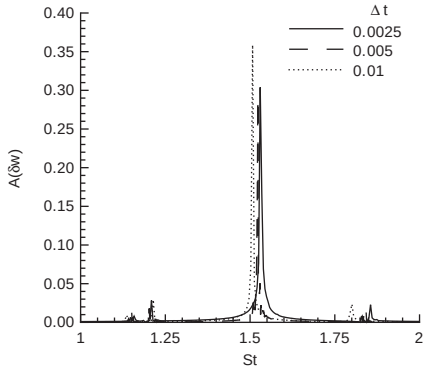

Fig. 19. Spectrum of panel fluctuations ($M_\infty = 0.8$, $\lambda = 500$).

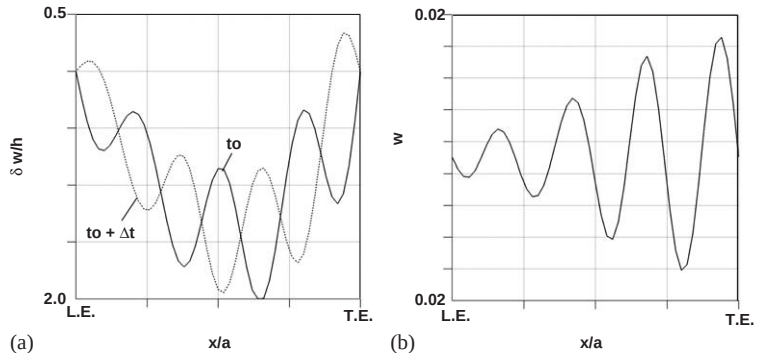

Fig. 20. Instantaneous panel shape (a) and vertical velocity (b) ($M_\infty = 0.8$, $\lambda = 500$, $\Delta t = 0.28$).

estimated convection speed and wavelength of these disturbances are $c_r = 0.47U_\infty$ and $\lambda = 0.25a \approx 9.2\delta$, respectively. The corresponding dominant frequency, obtained from the surface pressure signal at $x/a = 2.5$, was $\mathrm{St} = 1.9$. Comparison of this frequency with the baseline neutral stability for a flat-plate boundary layer is shown in Fig. 13. The computed frequency ($\beta_r \delta^*/U_\infty = 0.11$) lies within the range of unstable values indicating that the observed travelling wave flutter arises due to the amplification of T–S waves along the flexible panel. As demonstrated below, this *convective* instability subsides as the Reynolds number is reduced below a critical value.

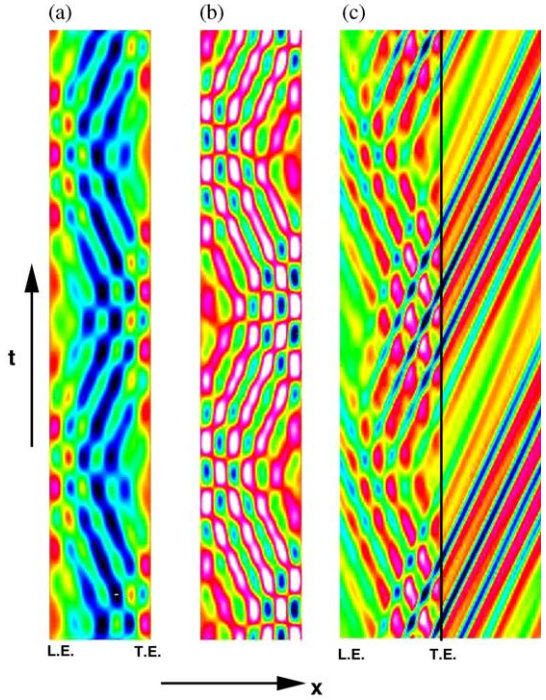

Fig. 21. x–t Diagram of panel deflection (a) transverse velocity (b) and surface pressure (c) ($M_\infty = 0.8$, $\lambda = 500$).

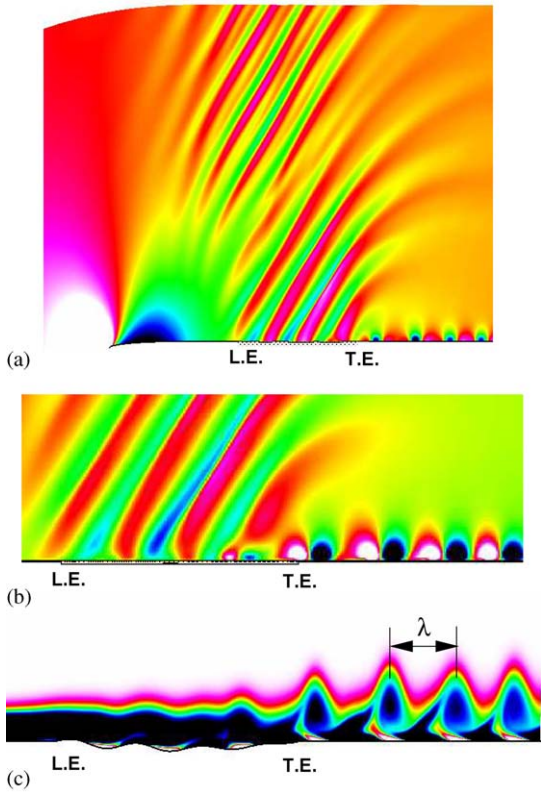

Fig. 22. Instantaneous flow structure above flexible panel in terms of contours of (a) pressure, (b) normal velocity and (c) spanwise vorticity. The vertical scale in (c) has been enlarged by a factor of 10 ($M_\infty = 0.8$, $\lambda = 500$).

The fluctuating flow field above the panel is shown in Figs. 23 and 24 in terms of the pressure and velocity perturbations. In accordance with the instantaneous flow structure previously described, significant acoustic radiation is observed above the panel (Fig. 23). Also apparent from the figure is the convective character of the boundary-layer instability along the vibrating surface, as evidenced by the increase in strength of the observed structures near the panel trailing edge. This behavior is made more clear by examination of the overall growth of the streamwise velocity fluctuations at a height $z/a = 0.07$, shown in Fig. 24(a). At this Mach number, the velocity fluctuations are considerably larger than those encountered in the low-speed case, with maximum value of $\sqrt{\overline{u'^2}}$ approximately equal to 0.13 at $z/\delta \approx 0.33$ (Fig. 24(b)).

The effectiveness of the far-field boundary treatment which employs the high-order low-pass filter in conjunction with a buffer region of rapid mesh stretching (see Fig. 2) is examined here in terms of the evolution of the velocity fluctuations. Fig. 25 displays the variation in the streamwise direction of the velocity perturbation $\sqrt{\overline{w'^2}}$ at $z/a = 0.07$. Downstream of the region of interest ($x/a > 2.5$), the fluctuations are observed to decay very quickly. By $x/a = 5.0$, which corresponds approximately to 16 grid points into the buffer zone, the fluctuations have been reduced by two orders of magnitude. It can also be noticed that no significant reflections appear within the fine-mesh region.

Effects of spatial and temporal numerical resolution. A limited investigation of numerical resolution effects is presented for $M_\infty = 0.8$ since this case is characterized by a higher-mode deflection and higher fluctuating frequencies on the panel. The effect of spatial resolution on the mean panel deflection and mean surface pressure is shown in Figs. 26 and 27, respectively. The doubling of mesh points in the streamwise direction (Grid 2) results in small reduction in the maximum mean deflection of the panel. The mean surface pressure displays only small differences, in particular near the

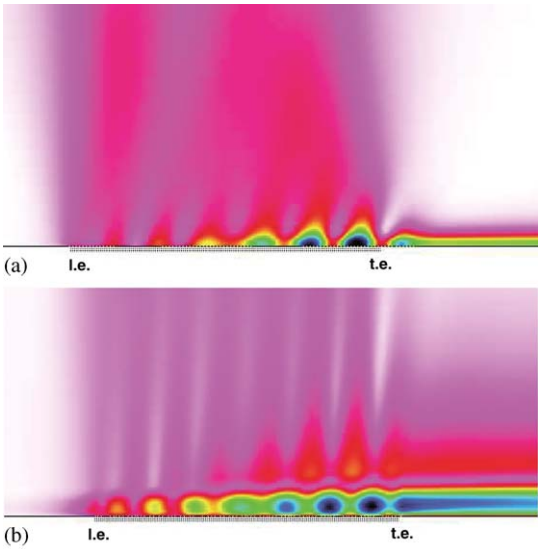

Fig. 23. Contours of RMS-pressure fluctuations (a) and streamwise velocity (b) above the panel ($M_\infty = 0.8$, $\lambda = 500$).

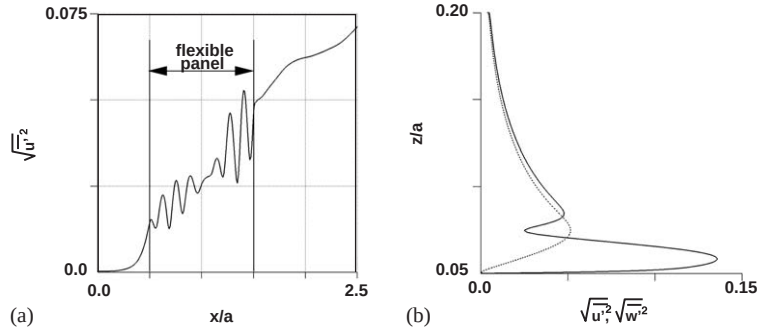

Fig. 24. Boundary-layer velocity fluctuations ($M_\infty = 0.8$, $\lambda = 500$).

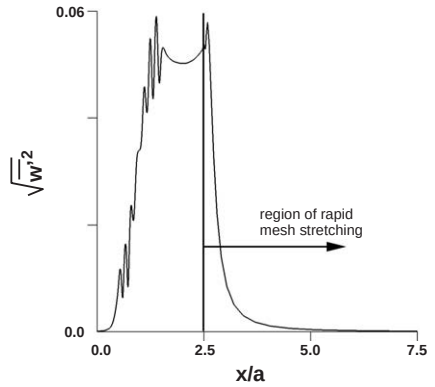

Fig. 25. Decay of boundary-layer velocity fluctuations in buffer zone ($M_\infty = 0.8$, $\lambda = 500$).

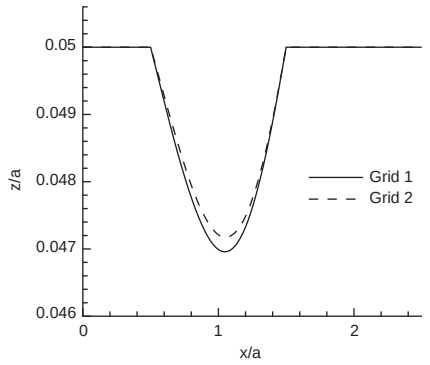

Fig. 26. Effect of spatial resolution on mean panel deflection ($M_\infty = 0.8$, $\lambda = 500$).

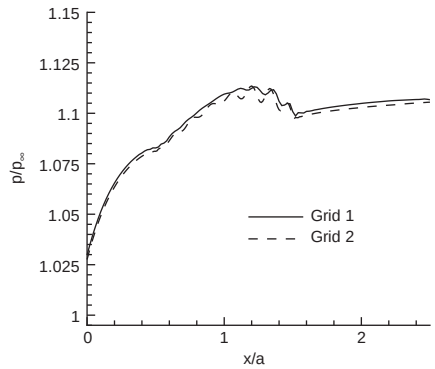

Fig. 27. Effect of spatial resolution on mean surface pressure ($M_\infty = 0.8$, $\lambda = 500$).

trailing-edge region of the panel. In addition, examination of the instantaneous flow fields obtained with both grids (not shown) revealed the same qualitative flow behavior.

The effect of computational time step Δt on the dominant frequency of the panel fluctuations at the quarter-chord location is given in Fig. 19. These results correspond to the finer mesh (Grid 2). The highest Δt displays a reduction in frequency of 1.5% and an increase in amplitude of 13%. However, the other two solutions are in much closer agreement with each other. Therefore, a time step $\Delta t = 0.005$ is considered to be adequate for the present simulations. Nonetheless,

for improved accuracy, the results presented above for the flow structure were obtained using $\Delta t = 0.0025$ which corresponds approximately to 264 time steps per cycle of oscillation.

Parametric effects. The effect of dynamic pressure on the fluid–structure interaction is shown in Figs. 14–16. For $\lambda \leqslant 200.0$, the panel exhibits a static instability (divergence) with increasing deformation as a function of dynamic pressure. For $\lambda = 300$, the onset of travelling-wave flutter is observed (Fig. 16), a process which is accompanied by a reduction in the mean panel deflections (Fig. 14). Further increase in λ results in higher amplitude and velocity fluctuations, however, the basic travelling flutter dynamics remained qualitatively unaltered.

Since for $M_\infty = 0.8$ the rigid-plate solutions displayed a residual streamwise pressure variation in the panel region (see Fig. 3 and Table 1), the effect of the prescribed constant cavity pressure p_c was investigated. For this purpose, the ratio p_c/p_∞ was varied from 0.92 to 1.0. It should be noted that for the baseline case considered previously the cavity pressure was set equal to $0.982p_\infty$. Fig. 28 shows the history of the transverse oscillations at the panel $\frac{3}{4}$-chord location for several values of p_c. As expected, the mean deflections increased with higher cavity pressure. For $p_c/p_\infty = 0.92$ and 0.94, travelling wave flutter is observed. For a sufficiently high cavity pressure ($p_c/p_\infty = 1$), flutter disappears and aeroelastic divergence (with positive deflection) occurs instead. Since this upward stationary deformation produces a favorable pressure gradient over a portion of the panel the boundary-layer instability waves are suppressed and a steady solution is achieved. For the lowest value of p_c considered, the panel exhibits significant downward deformation and the flutter amplitude is markedly diminished. However, residual oscillations ($(\delta w/h)_{\text{amp}} \approx 0.35$) remain despite the large mean deflection which increases the panel effective stiffness through the in-plane (membrane) stresses. By comparison of the upward- and downward-deflected solutions, it is clear that the divergence process is not so symmetric as in previously reported inviscid results (Gordnier and Visbal 2000). This bias is introduced in the present viscous case by the response of the boundary layer to the streamwise adverse pressure gradient induced by the panel downward deflection. This adverse pressure gradient promotes the amplification of T–S waves and their coupling with the panel flexural response. The present results also serve to point out the sensitivity in the response of the fluid/structural system to the difference in mean pressure across the panel. This clearly has implications for the comparison with experimental simulations and points the need for further analysis of the cavity characteristics.

The effect of Reynolds number on the observed travelling wave flutter is shown in Fig. 17 in terms of the transverse oscillation amplitude at the $\frac{3}{4}$-chord location. It is apparent that as Re_δ^* decreases below a critical value, the flutter phenomena disappears (i.e., $(\delta w/h)_{\text{amp}} = 0$) and only a static aeroelastic divergence of the panel remains (not shown). This behavior, which is entirely different from the $M_\infty = 0.2$ case, reinforces the explanation put forth earlier regarding the origin of the observed dynamic aeroelastic instability, i.e., the travelling flexural deflections are generated by the coupling with the boundary-layer instability waves.

The last parametric effects considered were the impact of the structural boundary conditions at the edges of the panel and the panel thickness. For this purpose, calculations were performed using clamped-edge conditions and a thicker panel with $h/a = 0.004$. Both of these modifications increase the effective flexural rigidity of the elastic panel. Although the results are not included here, the nature of the previously discussed travelling wave flutter was found to remain qualitatively unaltered for either clamped conditions or a thicker panel.

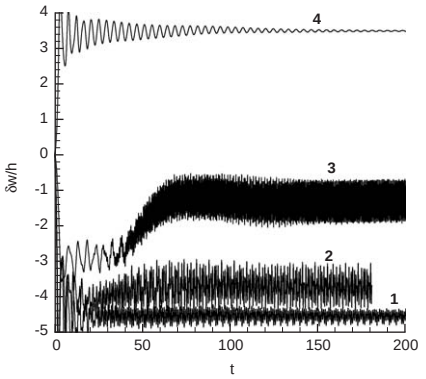

Fig. 28. Effect of cavity pressure on panel deflection at the $\frac{3}{4}$-chord point ($M_\infty = 0.8$, $\lambda = 500$). Curves 1–4 correspond to $p_c/p_\infty = 0.92$, 0.94, 0.982, 1.0, respectively.

5. Conclusions

The complex self-sustained oscillations arising in a transitional boundary layer flowing over a flexible finite panel were investigated numerically. The flowfields were obtained by solving the full compressible Navier–Stokes equations employing a recently developed high-order implicit solver. The code incorporates sixth-order compact spatial differences in conjunction with a tenth-order Pade-type low-pass spatial filter which eliminates odd-even modes. The solver attains sixth-order spatial and second-order temporal accuracy through the use of an iterative approximately factored time-marching scheme. Superior accuracy on deforming meshes is maintained by the proper treatment of the time-varying curvilinear transformation metrics. The flexible panel mechanics was described by means of the nonlinear von Karman plate equations which were solved using a previously validated finite-difference procedure. The fluid and structural solvers were coupled implicitly in order to eliminate numerical errors arising from lagged boundary conditions at the fluid–structure interface.

Computations were performed for two freestream Mach numbers ($M_\infty = 0.2, 0.8$) and for a Reynolds number of 10^5 based on the panel length. For both flow speeds, self-sustained oscillations developed in the combined fluid/structural system without application of any external forcing. The character of the observed flutter phenomena was found to be independent of the type of structural conditions (i.e., pinned or clamped) used at the panel edges. For $M_\infty = 0.2$, the panel transverse fluctuations appeared to be of an aeroelastic nature and did not disappear with decreasing Reynolds number. The oscillating surface, however, promoted instability waves in the boundary layer which were clearly observed downstream of the panel, with frequencies which fell within the neutral stability branches for an incompressible flat-plate boundary layer.

At $M_\infty = 0.8$, static divergence occurred for low values of the dynamic pressure, and despite the accompanying adverse streamwise pressure gradient induced by the panel downward deflection, a steady flow was attained (in the case of no applied external forcing). For higher values of dynamic pressure, a travelling-wave-flutter phenomenon emerged. These high-frequency flexural panel waves resulted in a pronounced acoustic radiation pattern above the fluttering plate. Downstream of the flexible panel, a regular train of vortical disturbances was observed with characteristic wavelength and frequency compatible with those of T–S instability. The travelling wave flutter appeared to originate from the coupling of the T–S waves with the panel high-mode transverse fluctuations. Unlike the low speed case, this convective instability ceases below a critical value of Reynolds number.

The effect of the cavity pressure underneath the panel was also investigated. It was found that small increases in cavity pressure could result in a static (upward) divergence. In this case, the favorable streamwise pressure gradient induced by the panel deflection completely suppressed the boundary-layer instability waves, and a steady solution was attained. This sensitivity of the interaction to the cavity pressure clearly has implications for comparison with experimental simulations.

Finally, given the complexity and richness of this nonlinear dynamic system, further study should be pursued in order to evaluate the impact of turbulence, structural damping and three-dimensional effects on the various modes of instability.

Acknowledgements

The authors are grateful for AFOSR sponsorship under task monitored by Dr T. Beutner. This work was also supported in part by a grant of HPC time from the DoD HPC Shared Resource Centers at ARSC and NAVO.

References

Abdel-Motaglay, K., Chen, R., Mei, C., 1999. Nonlinear flutter of composite panels under yawed supersonic flow using finite elements. AIAA Journal 37 (9), 1025–1032.

Alpert, P., 1981. Implicit filtering in conjunction with explicit filtering. Journal of Computational Physics 44, 212–219.

Anderson, D., Tannehill, J., Pletcher, R., 1984. Computational Fluid Mechanics and Heat Transfer. McGraw-Hill Book Company, New York.

Beam, R., Warming, R., 1978. An implicit factored scheme for the compressible Navier–Stokes equations. AIAA Journal 16 (4), 393–402.

Bendiksen, O., Davis, G., 1995. Nonlinear traveling wave flutter of panels in transonic flow. AIAA 95-1486, April.

Benjamin, T., 1963. The threefold classification of unstable disturbances in flexible surfaces bounding inviscid flow. Journal of Fluid Mechanics 16, 436–450.

Buter, T., Reed, H.L., 1994. Boundary layer receptivity to freestream vorticity. Physics of Fluids 6, 3368–3379.

Carpenter, P., 1990. Status of transition delay using compliant walls. In: Viscous Drag Reduction in Boundary Layers. pp. 79–113.
Chia, C., 1980. Nonlinear Analysis of Plates. McGraw-Hill International Book Company, New York.
Davies, C., Carpenter, P., 1997. Numerical simulation of the evolution of Tollmien–Schlichting waves over finite compliant panels. Journal of Fluid Mechanics 335, 361–392.
Davis, G., Bendiksen, O., 1993. Transonic panel flutter. AIAA 93-1476, April.
Dowell, E., 1975. Aeroelasticity of Plates and Shells. Noordhoff International, Leiden.
Dowell, E.H., 1966. Nonlinear oscillations of a fluttering plate. AIAA Journal 4 (7), 1267–1275.
Dowell, E.H., 1970. Panel flutter: a review of the aeroelastic stability of plates and shells. AIAA Journal 8 (3), 385–399.
Fung, Y.C., 1965. Foundations of Solid Mechanics. Prentice-Hall, Inc., Englewood Cliffs, NJ.
Gad-el-Hak, M., 1986. Boundary-layer interactions with compliant coatings: an overview. Applied Mechanics Reviews 39, 511–523.
Gaitonde, D., Visbal, M., 1998. High-order schemes for Navier–Stokes equations: algorithm and implementation into FDL3DI. Technical Report. AFRL-VA-WP-TR-1998-3060, Air Force Research Laboratory, Wright-Patterson AFB.
Gaitonde, D., Visbal, M., 1999. Further development of a Navier–Stokes solution procedure based on higher-order formulas. AIAA Paper 99-0557, January.
Gaitonde, D., Shang, J., Young, J., 1997. Practical aspects of high-order accurate finite-volume schemes for electromagnetics. AIAA Paper 97-0363, January.
Gordnier, R.E., Fithen, R., 2001. Coupling of a nonlinear finite element structural method with a Navier–Stokes Solver. AIAA-2001-2853, June.
Gordnier, R.E., Visbal, M.R., 2000. Development of a three-dimensional viscous aeroelastic solver for nonlinear panel flutter. AIAA Paper 2000-2337.
Gordnier, R.E., Visbal, M.R., 2001. Computation of three-dimensional nonlinear panel flutter. AIAA Paper 2001-0571.
Humar, J.L., 1990. Dynamics of Structures. Prentice-Hall, Inc., Englewood Cliffs, NJ.
Jameson, A., Schmidt, W., Turkel, E., 1981. Numerical solutions of the Euler equations by a finite volume method using Runge–Kutta time stepping schemes. AIAA Paper 81-1259.
Kramer, M., 1957. Boundary-layer stabilization by disturbed damping. Journal of Aeronautical Science 24, 459.
Landahl, M., 1962. On the stability of a laminar incompressible boundary layer over a flexible surface. Journal of Fluid Mechanics 13, 609–632.
Lele, S., 1992. Compact finite difference schemes with spectral-like resolution. Journal of Computational Physics 103, 16–42.
Nydick, I., Friedmann, P., Zhong, X., 1995. Hypersonic panel flutter studies on curved panels. AIAA Paper 95-1485-CP.
Pulliam, T., 1986. Artificial dissipation models for the Euler equations. AIAA 24 (12), 1931–1940.
Pulliam, T., Chaussee, D., 1981. A diagonal form of an implicit approximate-factorization algorithm. Journal of Computational Physics 39 (2), 347–363.
Schlichting, H., 1968. Boundary-Layer Theory. McGraw-Hill Book Company, New York.
Thomas, P., Lombard, C., 1979. Geometric conservation law and its application to flow computations on moving grids. AIAA Journal 17 (10), 1030–1037.
Visbal, M., Gaitonde, D., 1998. High-order accurate methods for unsteady vortical flows on curvilinear meshes. AIAA Paper 98-0131, January.
Visbal, M., Gaitonde, D., 1999a. Computation of aeroacoustic fields on general geometries using compact-differencing and filtering schemes. AIAA Paper 99-3706, June.
Visbal, M., Gaitonde, D., 1999b. High-order accurate methods for complex unsteady subsonic flows. AIAA Journal 37 (10), 1231–1239.
Visbal, M., Gaitonde, D., 2001. Very high-order spatially implicit schemes for computational acoustics on curvilinear meshes. Journal of Computational Acoustics 9 (4), 1259–1286.
Visbal, M., Gordnier, R., 2000. A high-order flow solver for deforming and moving meshes. AIAA Paper 2000-2619, June.